

RESEARCH ARTICLE | MAY 15 2024

A new compact symmetric shear diamond anvil cell for *in situ* high-pressure-torsion studies

K. K. Pandey   ; H. K. Poswal 

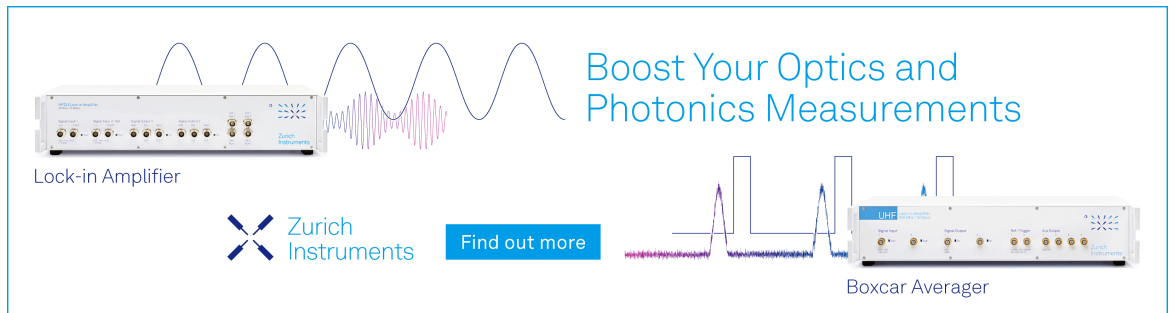


Rev. Sci. Instrum. 95, 053904 (2024)


<https://doi.org/10.1063/5.0193048>



Boost Your Optics and Photonics Measurements



Lock-in Amplifier



Find out more

Boxcar Averager

A new compact symmetric shear diamond anvil cell for *in situ* high-pressure-torsion studies

Cite as: Rev. Sci. Instrum. 95, 053904 (2024); doi: 10.1063/5.0193048

Submitted: 21 December 2023 • Accepted: 1 May 2024 •

Published Online: 15 May 2024



View Online



Export Citation



CrossMark

K. K. Pandey^{a)}  and H. K. Poswal^{b)} 

AFFILIATIONS

High Pressure and Synchrotron Radiation Physics Division, Bhabha Atomic Research Centre, Mumbai 400085, India and Homi Bhabha National Institute, Anushaktinagar, Mumbai 400094, India

^{a)} Author to whom correspondence should be addressed: kkpandey@barc.gov.in

^{b)} himanshu@barc.gov.in

ABSTRACT

In situ studies under severe plastic deformation at high pressures, employing shear diamond anvil cells, have recently gained much interest in the high-pressure community owing to their potential applications in material processing methods, mechanochemistry, and geophysics. These studies, combined with multi-scale computational simulations, provide important insights into the transient hierarchical microstructural evolution, structural phase transitions, and orientation relationship between parent and daughter phases and help establish the kinetics of strain-induced phase transitions under severe plastic deformation. The existing SDACs are mostly used in axial x-ray diffraction geometry due to geometrical constraints providing less reliable information about stress states and texture. Their asymmetric design also poses serious limitations to high-pressure shear studies on single crystals. To overcome these limitations, a new compact symmetric shear diamond anvil cell has been designed and developed for *in situ* high-pressure torsion studies on materials. The symmetric angular opening and short working distance in this new design help obtain a more reliable crystallographic orientation distribution function and lattice strain states up to a large Q range. Here, we present the advantages of the symmetric design with a few demonstrative studies.

Published under an exclusive license by AIP Publishing. <https://doi.org/10.1063/5.0193048>

I. INTRODUCTION

Severe plastic deformation (SPD) has been in use for ages for metal forming and synthesis of high-strength materials.^{1–5} The availability of precise characterization techniques in recent decades, such as scanning electron microscopy (SEM), transmission electron microscopy (TEM), electron backscatter diffraction (EBSD), and synchrotron-based micro x-ray diffraction (XRD), has made the SPD an even more effective tool for producing bulk ultrafine-grained and nanostructured materials with advanced mechanical and functional properties.^{6,7} Depending on the methodology and complex load-shear pathways that the material is subjected to, SPD can be used to introduce various kinds of lattice defects and unique microstructural features. High-pressure torsion (HPT), first introduced by Bridgman up to a few GPa pressures,^{8,9} is one of the classic techniques of SPD used for studying grain refinement, strain hardening, structural changes, polymorphism, and mechanochemistry. However, most of the studies performed using conventional tungsten carbide anvils are carried out *ex situ*, which is oblivious to micro-mechanical processes happening in

the system while under load-shear conditions. The shear strain estimated under HPT ($\gamma = 2\pi rN/h$, where r is the radial distance from the symmetry axis of rotation, N is the number of rotational turns of one anvil with respect to another, and h is the sample thickness)^{10,11} is based on the assumption of ideal contact friction conditions between the sample and anvils, which may not be correct. The pressure estimates under HPT calculated as force/area may also be inaccurate due to the presence of heterogeneities in stress states across anvil culet. These limitations do not allow any systematic quantitative study of processes under HPT.¹²

Combining the Bridgman method for high-pressure torsion and the concept of the diamond anvil cell developed in 1959,¹³ Blank *et al.* introduced the first shear diamond anvil cell (SDAC) in the 1980s,^{14,15} which not only provided an opportunity to increase the pressure by several tens of GPa but also facilitated *in situ* studies under HPT employing x-ray diffraction¹⁶ and Raman spectroscopy.¹⁷ The cell was designed with an additional degree of freedom of rotation of one of the anvils with respect to another, facilitating HPT in the sample. Figure 1 shows

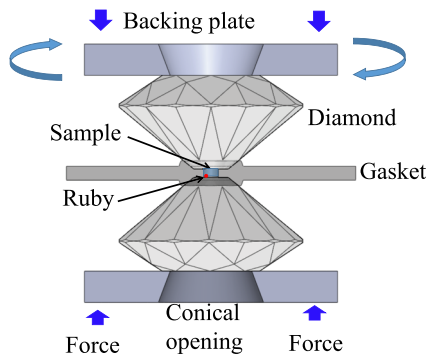


FIG. 1. Schematics of the shear diamond anvil cell.

the schematic of SDAC. Over the years, owing to the importance of *in situ* studies under high-pressure deformation, other research groups also developed their design of sophisticated high-pressure devices providing heterogeneous stress conditions^{18–23} and carried out *in situ* studies on materials ranging from elemental metals²⁴ and ceramics^{25,26} to geophysical and planetary materials^{27–31} bearing basic as well as applied scientific interest. Recently, HPT studies, although not *in situ*, have been extended to organic materials for the simulation of impacts by small solar system bodies.³²

These studies help establish the classification of HP phase transitions as pressure-induced, stress-induced, or plastic strain-induced.^{33,34} Among these, plastic strain-induced phase transitions where plastic strain acts like a time-like parameter are especially important for *in situ* HPT studies.^{35–37} In most of the *in situ* studies under HPT in SDAC, the primary focus has been the microstructural evolution, polymorphism, amorphization, nature of phase transition, and its mechanism, with little or no emphasis on the quantitative association of plastic strains to the phase transformation kinetics.

Levitas has given a multi-scale theoretical approach to explain the plastic strain-induced phase transitions and proposed a kinetic theory of these phase transitions as a function of the accumulated plastic strain, initiation pressure for the phase transformation under hydrostatic conditions, and complex load-shear conditions and transformed phase concentration.^{35,34,38} The first experimental validation of this theory has been published recently only with an example study on the $\alpha \rightarrow \omega$ phase transition in ultra-pure Zr.³⁹ Such studies open a new opportunity for the quantitative study of strain-induced PTs and reactions with applications to material synthesis and processing, mechanochemistry, and geophysics.

Even though the SDACs used for such studies^{17,22,39} are quite sophisticated, the reliability of quantitative estimation of elastic-plastic strains and texture, suffer from some or the other limitations of these DACs.

Some of the design limitations of the existing SDACs are as follows:

- (a) *Small angular opening of $\sim 30^\circ$ (4θ) at the data collection side, limiting the Q range of XRD data collection. This is a serious limitation for quantitative Rietveld analysis⁴⁹ of XRD*

patterns for the estimation of reliable crystallographic and microstructural parameters.

- (b) *Asymmetric working distance at the two sides of SDAC, viz. ~ 30 mm at one side and ~ 120 mm at other side, which allows XRD data collection in the axial geometry only. Due to this limitation, the XRD measurements in SDACs are mostly carried out in axial geometry, where the load axis is parallel to the incident x-ray beam. In this geometry, the diffraction condition is satisfied for the planes whose normal is mostly perpendicular to the load axis. Hence, the lattice strains are under-estimated in axial geometry. To overcome this limitation, the XRD data can be recorded in radial geometry (load axis perpendicular to the incident x-ray beam)^{40–42} covering all stress states at different azimuthal angles of Debye rings. However, the radial geometry is out of the question here as it would provide averaged information across anvil culet diameter with no insights into the pressure profile and stress heterogeneities in the sample across culet diameter. Recently, methodologies have been developed by combining experimental observations and finite element method (FEM) to obtain more reliable stress estimates in DAC.⁴³ Another possibility is to carry out the XRD measurements in oblique angle geometry (load axis at some angle between 0° and 90° with respect to the incident x-ray beam); however, the asymmetric design of existing SDACs does not allow such measurements. Another disadvantage with axial geometry is the restricted coverage of the pole figure,⁴⁴ which limits the reliability of quantitative texture estimation. In addition, with asymmetric working distance at both sides, existing SDACs allow only single-sided spectroscopy measurements, such as micro-Raman or Brillouin scattering measurements, that too in the backscattered geometry. Under HPT conditions, these spectroscopy measurements at both sides of SDACs become important to estimate stress states at both the sample-anvil contact surfaces.*
- (c) *No possibility of simultaneous control over load and shear. During plastic deformation under shear sample, usually pressure reduces in the sample due to thinning, which needs to be compensated simultaneously to carry out measurements at constant load conditions.*

To overcome these limitations, a new compact symmetric SDAC (SSDAC) has been design and developed. The advantages of the new design are as follows: wider angular opening of $\sim 60^\circ$ (4θ); *symmetric design with equal working distance of < 20 mm at both sides, allowing XRD data collection to large Q range in axial and oblique geometry; better quantitative texture analysis with extended pole figure convergence; relatively higher numerical aperture of 0.5 for better collection efficiency of spectroscopic data; simultaneous control over load and shear using membrane and stepper motor drive, respectively; and compact design facilitating easy handling and usage at XRD and spectroscopic facilities.* The cell is designed with Boehler Amlax type anvils⁴⁵ and can be used for unlimited rotations at pressures as high as 50 GPa. The pressure range may be further increased using different anvil designs and suitable backing seats. The salient features of this new design and a few example studies have been presented in the following sections to demonstrate the capabilities of the new SSDAC.

II. DESIGN AND SALIENT FEATURES OF SSDAC

The new SSDAC has been designed with symmetric angular openings on both sides with the provision of rotation of one of the diamond anvils with respect to another. As the SSDAC is to be used for *in situ* XRD and spectroscopic studies, special consideration is given to large symmetric angular openings, short working distance, and coaxial stability under high load/shear conditions. Simultaneous loading and rotation of the piston with respect to the cylinder requires a ball bearing between the piston and the pressure plate to reduce friction. However, it poses restrictions on the working distance and angular opening of the cell. We have overcome this limitation by designing a custom ball bearing for the rotation mechanism. A piston-cylinder assembly is chosen for better translational alignment and coaxial stability of the diamond anvils during loading and rotation. For SSDAC to work properly, the runout of the piston should be as small as possible. We have kept it less than 5 μm . Surface roughness and waviness of the cylindrical surfaces have also been kept as small as possible. The exploded view of the SSDAC design is shown in Fig. 2. The SSDAC and conical diamond anvils have been manufactured by M/s Somdev Instruments Pvt. Ltd. India.⁵⁰

A. Load and torsion mechanism

The SSDAC is designed with an integrated gear mechanism and motorized rotation with a stepper motor. The gear mechanism rotates the anvil mounted on the piston, whereas the anvil mounted on the cylinder remains fixed. There are two mechanisms for applying the load: (i) manual loading using four screws (two right-handed and two left-handed), which press the cylinder part against a load-applying plate with threaded holes for the screws and (ii) gas pressure loading using a double diaphragm membrane for applying the load from the opposite side of the gear assembly rotation mechanism with an additional thrust plate (Fig. 3). In manual loading, Belleville spring washers are used, while membrane loading is done without any Belleville washers. The gear ratio between the stepper motor and anvil rotation is 1:180, which provides

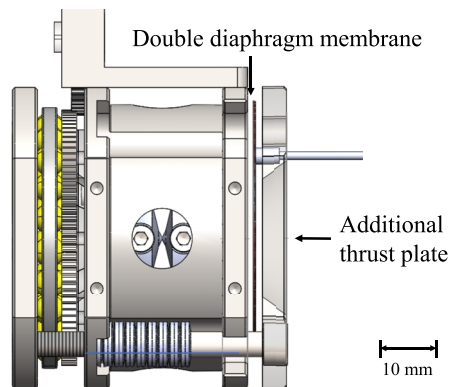


FIG. 3. Double diaphragm membrane with an additional thrust plate for applying load in the SSDAC in gas pressure drive mode.

quasi-static shear conditions at very low-speed rotations (<1 rpm). The stepper motor with gear provides a maximum torque of 4 Nm for the rotation of the piston, which, as per our experience, is sufficient for the rotation of the piston anvil even under high load conditions. The design of the motorized mechanism and full assembly of SSDAC are shown in Fig. 4.

B. Tilt and translation adjustment for both anvils

One of the primary requirements of SDAC is to align the diamond anvils with respect to each other and with respect to the rotation axis of the SDAC. To achieve this, both the anvils are provided with tilt and translation adjustments, as shown in Fig. 2. The backing seat for both the anvils for the piston and the cylinder is designed with a hemispherical rocker for tilt adjustment and a cylindrical backing plate for Böhler-type diamond anvils, mountable within the hemispherical rockers with provision for translational alignment. Both the piston and cylinder are provided with fourfold holes for the translational alignment of the anvils (Fig. 5).

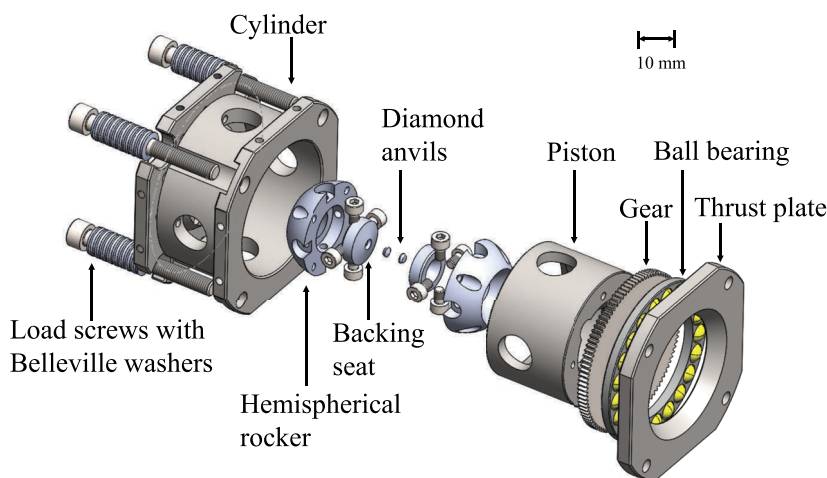


FIG. 2. Exploded view of the newly designed and developed compact SSDAC.

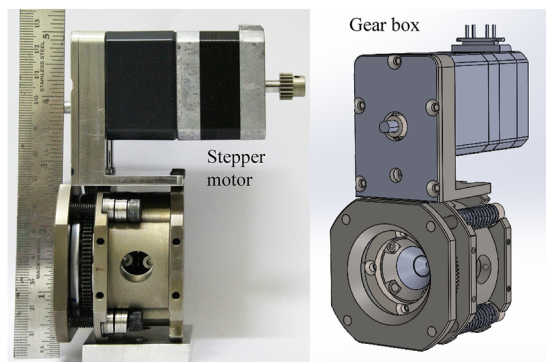


FIG. 4. Motorized assembly of the compact SSDAC.

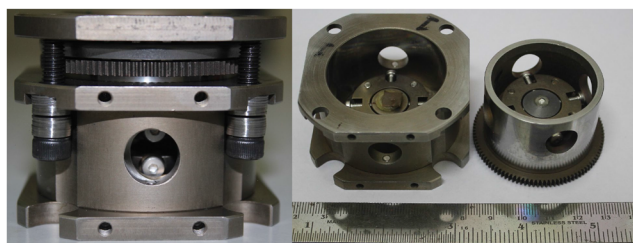


FIG. 5. Piston and cylinder of the SSDAC.

C. Symmetric x-ray opening

Existing SDACs^{17,22,23} are mostly piston-cylinder type, where the load is applied mechanically through a lever or screw mechanism. Due to the technical requirements, these SDACs have asymmetric x-ray openings at the piston and cylinder sides. In order to carry out oblique angle XRD measurements, the SDAC needs to be tilted with respect to the incident x-ray beam; however, very limited angular opening at the piston side ($\sim 2^\circ$) does not allow these measurements. Although high-pressure rotational deformation apparatus developed by Nomura *et al.*²³ can be used for oblique angle XRD and x-ray laminography with a large lateral opening, the spatial resolution of stress heterogeneities within the sample may be compromised. We have overcome these limitations by designing an SDAC with a symmetric opening on both sides. This new design provides a compact symmetric opening of $60^\circ (4\theta)$ at both sides, facilitating oblique angle XRD measurements from -30° to $+30^\circ$. With the symmetric x-ray opening, the SSDAC can also be used for single-crystal XRD measurements under high-pressure torsion.

D. Compact design

The SSDAC has been designed to be as compact as possible without compromising its capabilities. To have a compact size of SSDAC and good stability, the piston cylinder engagement is maximized by keeping the anvil from mounting assembly inside the piston. The overall diameter of the piston-cylinder is ~ 53 mm. The working distance at both sides of the piston-cylinder assembly is < 20 mm on both sides using objectives of outer diameter

~ 26 mm, such as Olympus SLMPlan 20 \times . This facilitates spatially resolved micro-Raman studies across samples from both sides. This is also useful for recording high spatially resolved ruby fluorescence images at both sides of the sample implementing the recently developed displacement field methodology.⁴⁸ With these measurements, the plastic flow of the sample at the sample-anvil contact surface and actual torsion in the sample can be obtained quantitatively. The overall weight of the entire assembly, including the stepper motor for rotation and the gear mechanism, is ~ 1 kg. The footprint of DAC is ~ 60 mm \times 50 mm. With the compact design, the SSDAC can be easily carried and mounted at different laboratory-based experimental facilities and synchrotron facilities.

III. ALIGNMENT AND TESTING

The anvils of the SSDAC need to be aligned with respect to each other and the rotation axis of the piston-cylinder assembly of the SSDAC. For this, first the anvil was mounted on the piston side only, and it was aligned with respect to the rotation axis using a monocular zoom microscope and laser reflection method, as shown in Fig. 6. Once this anvil is aligned, the other anvil is mounted on the cylinder side and aligned with respect to the already mounted anvil under a microscope using interference fringe method.

To confirm the stability of alignment under load conditions, an Ni gasket was loaded in the SSDAC along with several ruby particles of size $\sim 2 - 5$ μm at the sample-anvil contact surface and was subjected to uniaxial compression. Under the given load condition, the pressure distribution in the SSDAC was estimated using the ruby fluorescence method⁴⁶ and the shift in the diamond Raman peak.⁴⁷ As shown in Fig. 7, the pressure distribution shows a symmetric conical shape, which confirms the alignment of anvils under high load conditions. The maximum pressure observed at the center of culet was ~ 20 GPa.

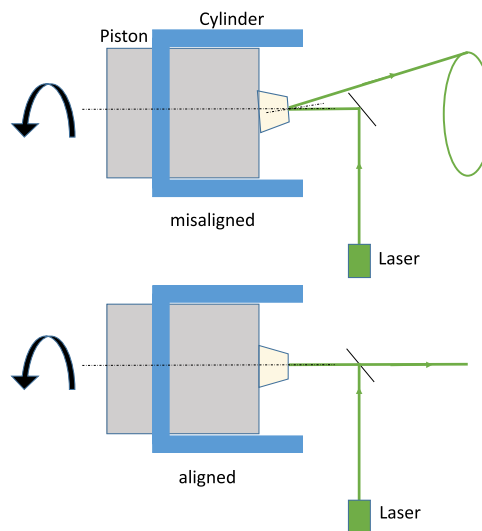


FIG. 6. Schematic of the arrangement for anvil alignment.

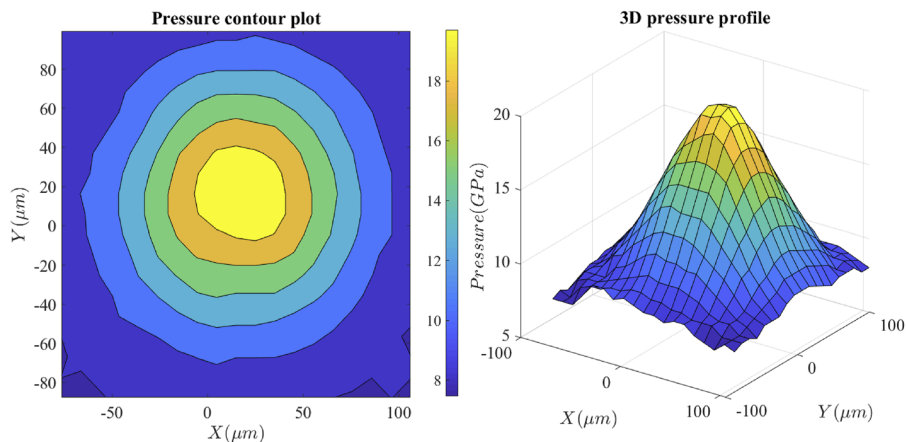


FIG. 7. Pressure distribution in the Ni gasket at a given load condition in the SSDAC.

IV. DEMONSTRATIVE STUDIES

A. Oblique angle XRD measurements

With symmetric x-ray openings at both sides, the newly developed SSDAC can be used for oblique angle XRD measurements, providing more reliable stress estimates besides capturing stress heterogeneities and pressure profiles across anvil culet. The geometry of oblique angle XRD is shown in Fig. 8. The symmetric XRD opening of $\sim \pm 30^\circ$ in the new design of SSDAC allows oblique angle XRD measurements up to $\sim 28^\circ$. To compare the lattice strain estimation in the axial and oblique angle measurements, a Zr sheet of thickness $\sim 100 \mu\text{m}$ was loaded in the SSDAC and subjected to some uni-axial load, such that the pressure at the center of the culet was restricted to $\sim 2 \text{ GPa}$ to avoid $\alpha \rightarrow \omega$ phase transition in Zr. Under the same load condition, XRD measurements were carried out in axial geometry and at oblique angles of 24° . The measurements were carried out

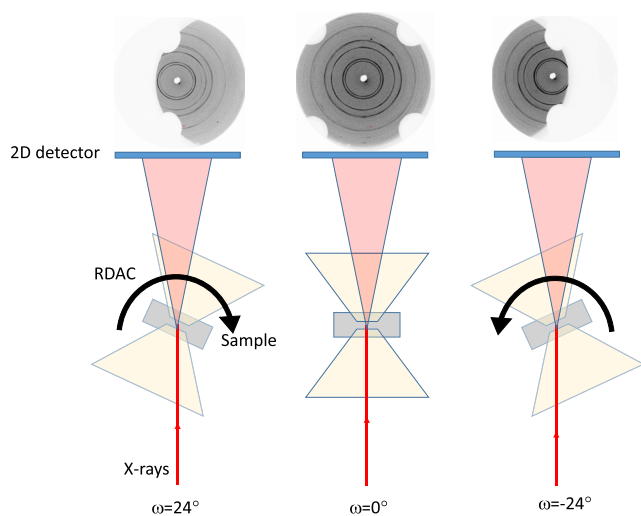


FIG. 8. Schematic of oblique angle XRD measurements in the SSDAC.

using micro-focused monochromatic x rays ($\lambda = 0.6649 \text{ \AA}$; FWHM = $10 \mu\text{m}$) at Extreme conditions XRD (ECXRD) beamline, BL-11 at Indus-2 synchrotron source, India⁵¹ (Fig. 9).

To maintain the same sample-to-detector distance, the sample was aligned at the rotation axis of the sample stages at the beamline, which is pre-aligned with respect to the incident x rays. The 2D diffraction images in these geometries were integrated into several azimuthal angle sectors of 5° and analyzed using MAUD software.⁵² As shown in Figs. 10 and 11, the cake integration of diffraction peaks in axial geometry is almost straight implying the same lattice strain in all azimuthal directions, whereas for oblique angle XRD, the diffraction peaks exhibit curvature, which is a signature of different lattice strains at different azimuthal directions.

To estimate deviatoric stresses at the center, the macro-stress components ($\sigma_{11}, \sigma_{22}, \sigma_{33}$) were refined using the tri-axial model as implemented in MAUD software. Here, σ_{33} is along the load axis, and σ_{11} and σ_{22} are perpendicular to the load axis in the 0° azimuthal plane and perpendicular to this plane, respectively. For the axial geometry, thus obtained, macro-stress components are found to be very close to zero ($\sigma_{33} = -0.003 \pm 0.001 \text{ GPa}$ and $\sigma_{11} = \sigma_{22} = 0.0015 \pm 0.001 \text{ GPa}$), which is not consistent with the expected macro-stresses during plastic deformation in the SSDAC. In the plastic deformation regime in DAC, the deviatoric

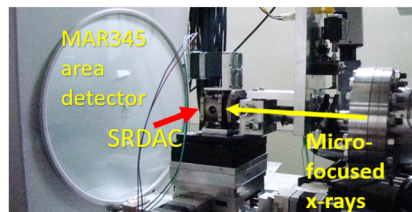


FIG. 9. Experimental station at the Extreme conditions XRD (ECXRD) beamline, BL-11 at Indus-2 synchrotron source, India,⁵¹ with the SSDAC mounted at the sample stage.

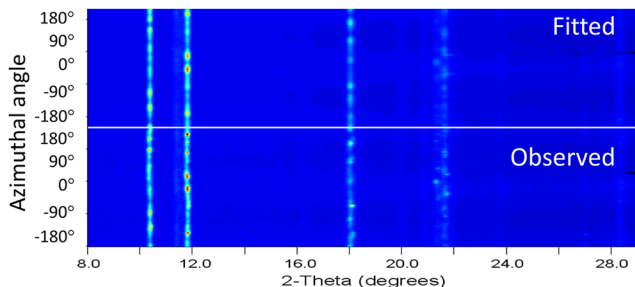


FIG. 10. Observed and fitted cake integration of the XRD image of α Zr recorded at ~ 2 GPa in axial geometry.

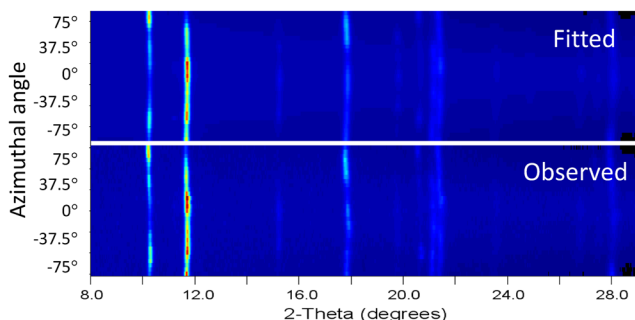


FIG. 11. Observed and fitted cake integration of the XRD image of α -Zr recorded ~ 2 GPa in oblique geometry.

stress should correspond to the yield strength of the material as $\sigma_y = |\sigma_{33} - \sigma_{11}|$. For oblique geometry, the macro-stress components are found to be $\sigma_{33} = -0.8 \pm 0.008$ GPa and $\sigma_{11} = \sigma_{22} = 0.4 \pm 0.008$ GPa. Here, we have used the constraint $\sigma_{11} = \sigma_{22} = -0.5\sigma_{33}$, which is a valid assumption at the symmetry axis of the SSDAC. The thus obtained yield strength of α -Zr is 1.2 GPa at ~ 2 GPa, which is consistent with the earlier reported values.⁴³

Due to the larger 2θ range of up to 30° , as shown in Fig. 11, the extent of curvature does not appear much, although it is significant enough for refinement. The maximum curvature in the cake integration will be observable in radial diffraction, where incident x rays are perpendicular to the load axis, whereas in our SDAC, the maximum oblique angle possible is 28° so the extent of curvature will be relatively less. Obtaining stress components at higher pressures might have been more convincing; however, the curvature depends on the elastic modulus and yield strength of material, which vary weakly with pressure. So, even at higher pressures, the curvature in cake integration will not be much. Nevertheless, we have performed additional oblique angle XRD measurement up to ~ 40 GPa. As Zr is a relatively soft material, achieving such high pressures in unconstrained compression in our SDAC was difficult due to material flow, and we carried out the study on a tungsten (W) gasket. We also loaded gold (Au) powder on the sample-anvil contact surface to obtain pressure at the center of our SDAC. The load axis of the SDAC was tilted to 28° with respect to incident x rays for the oblique angle XRD measurement. The XRD measurements were carried out using micro-focused monochromatic x rays of wavelength

$\lambda = 0.4953 \text{ \AA}$. The observed and fitted cake integration of the XRD data of W and Au is shown in Fig. 12. The deviatoric stresses in W, obtained using MAUD analysis, were $\sigma_{33} = -4.02 \pm 0.001$ GPa and $\sigma_{11} = \sigma_{22} = 2.01 \pm 0.001$ GPa at ~ 40 GPa. Here, one can again see that the curvature in cake integration (Fig. 12) is not quite large but the obtained deviatoric stresses are significant. Using these stress components, the yield strength of W at ~ 40 GPa is found to be $\sigma_y = 6.03$ GPa, which is consistent with the earlier reported pressure-dependent yield strength of tungsten ($1.8 + 0.1p$ GPa, where p is pressure in GPa).⁵³

Hence, the oblique geometry XRD measurements, possible with our newly designed SSDAC, provide more reliable quantitative estimates of macro-stresses as compared to the axial geometry. These macro-stress components can be used to estimate the pressure-dependent yield strength of materials. It is worth mentioning here that even the oblique angle XRD measurements would give information averaged over the oblique thickness of the sample parallel to the x-ray beam. However, as the sample thickness (h) in the SDAC is usually small ($< 50 \mu\text{m}$) and the oblique angle (ω) is 24° , the averaging is over a length scale of $h \cdot \tan(\omega)$, which turns out to be $< 25 \mu\text{m}$. In the future, new methodologies combining experiments and macro-FEM simulations will be developed similar to Ref. 43 for a more precise quantitative estimate of stress states and their heterogeneities with the oblique angle XRD measurements.

B. Texture studies with higher pole figure convergence

The study of texture evolution under plastic straining provides vital insights into the deformation mechanism, and in the case of phase transitions, it helps establish the orientation relationship between the parent and daughter phases. For quantitative studies, the accuracy of texture parameters is important, which depends on the pole figure convergence in the XRD measurements. In axial geometry, the pole figure convergence is limited, as shown in Fig. 13(a).

The pole figure convergence can be improved by recording XRD images at different ω angles. With the new design of the

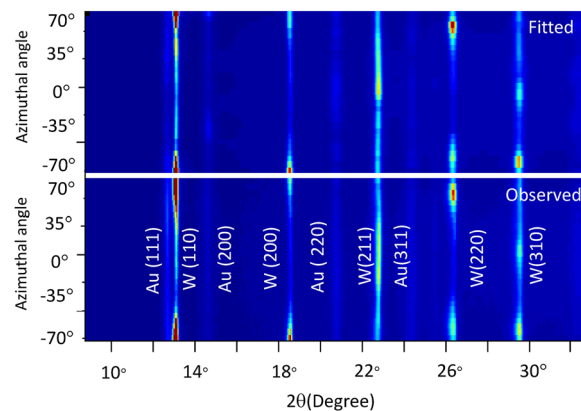


FIG. 12. Observed and fitted cake integration of the XRD image of tungsten at ~ 40 GPa recorded in oblique geometry with $\omega = 28^\circ$.

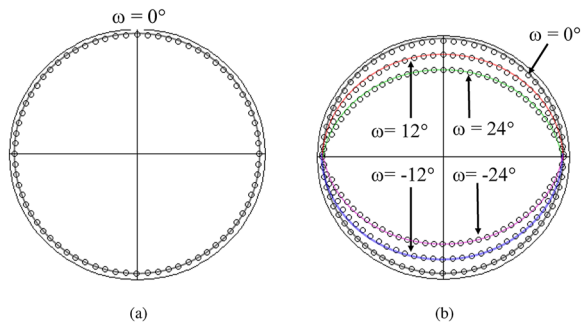


FIG. 13. (a) Pole figure convergence for the XRD data recorded in axial geometry with $\omega = 0^\circ$; (b) pole figure convergence for the XRD data recorded at different ω angles ranging from -24° to 24° about the axial geometry.

SSDAC, XRD images can be recorded at different ω angles as far as the geometrical constraints allow. As a demonstrative study, we recorded XRD images of the hexagonal α Zr sample loaded in the SSDAC with ω angles ranging from -24° to $+24^\circ$ in steps of 4° . Figure 13(b) shows the pole figure convergence using all the diffraction data recorded at different ω angles. The quantitative texture analysis has been carried out using these diffraction data employing the E-WIMV texture model as implemented in MAUD software. Figures 14 and 15 show the reconstructed pole figures of a few diffraction planes and inverse pole figures, respectively. The analysis shows the strong preferred orientation of (0002) planes along the load axis. The texture has nearly fiber symmetry, which is expected, even though the analysis has been done without imposing any symmetry on the texture model.

C. Displacement field measurements

For displacement field measurements in DAC/SDAC, a digital image correlation-based methodology has been recently developed.⁴⁸ These measurements are very important to obtain adhesion zones and relative sliding between the sample and anvil, which can be used as the boundary conditions for finite element method simulations of the processes in DAC/SDAC instead of hypothetical friction conditions. In this method, several ruby particles of size ~ 2 to $5 \mu\text{m}$ are placed at the sample-anvil contact surface at both

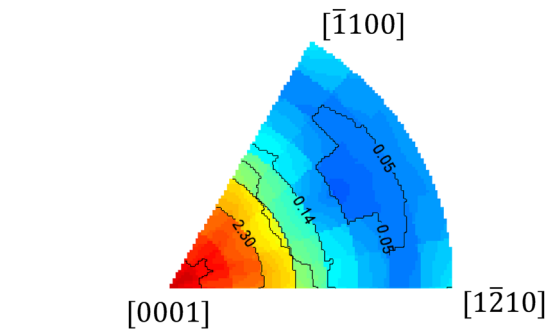


FIG. 15. Inverse pole figure obtained from texture analysis of the XRD data of hexagonal α Zr recorded at ~ 2 GPa exhibiting strong preferred orientation along the [0001] direction.

sides of DAC/SDAC, and magnified ruby fluorescence images are recorded from these ruby particles before and after load/shear conditions. These images are analyzed using the digital image correlation method to find out the displacement field in DAC/SDAC. For better accuracy of measurements, the resolution of fluorescence images should be as good as possible.

The optical setup for getting these images has to be designed for both sides as per the available working distance. At best, the resolution of the image is diffraction-limited and depends on the numerical aperture (NA) of the optics. For better resolution, the optical aperture should be as large as possible and the focal length of the objective lens should be as small as possible. Existing designs of the SDAC are asymmetric with longer working distance (typically, >100 mm) and smaller aperture (typically <10 mm) at one side (piston side), which limits the resolution of the image to $\sim 7 \mu\text{m}$ for the spectral range of ruby fluorescence. Whereas at the cylinder side, short working distance allows standard objectives, with NA ~ 0.28 (focal length: 35 mm) providing lateral resolution of $\sim 1.2 \mu\text{m}$. To demonstrate the effect of the optical system with a different focal length of objective lens on the image quality of ruby fluorescence image, ruby particles of size ~ 2 – $5 \mu\text{m}$ were spread at both the sample-anvil contact surfaces on a steel gasket mounted on our SDAC. For recording the ruby fluorescence image, an optical arrangement was made at both sides of the SDAC, as described in

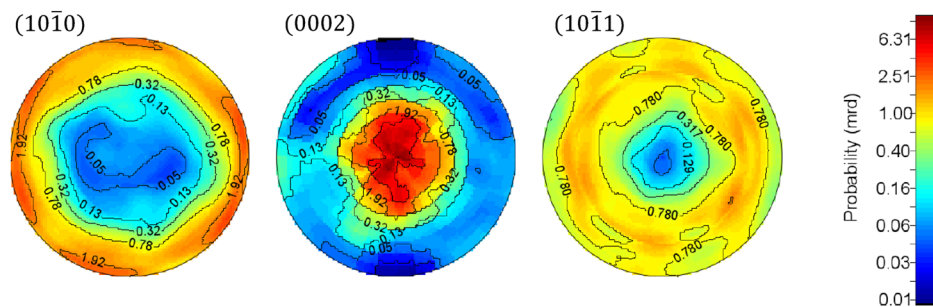


FIG. 14. Reconstructed pole figure of the $(10\bar{1}0)$, (0002) , and $(10\bar{1}1)$ diffraction planes using the XRD data of hexagonal α Zr recorded at ~ 2 GPa at different ω angles about the axial geometry.

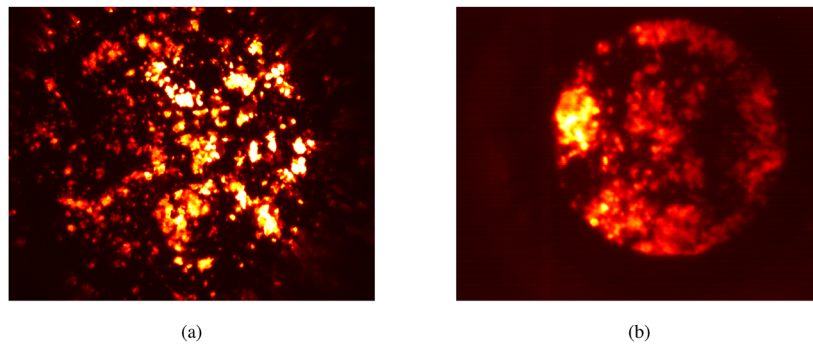


FIG. 16. Optical image of fluorescing ruby particles dispersed on the sample-anvil contact surface in the SSDAC recorded with two optical imaging systems having different objective focal length of (a) 20 mm with numerical aperture of 0.28 and (b) 120 mm with an numerical aperture of 0.04.

Ref. 48, with a 5 mW, 405 nm diode laser for fluorescence excitation in ruby particles. At one side, a 20 mm focal length objective was used, and at the other side, a 120 mm focal length objective was used. Ruby fluorescence was recorded at both sides. Figures 16(a) and 16(b) show the ruby fluorescence images recorded with the optical setup of focal lengths 20 and 120 mm, respectively, which demonstrates the difference in resolution.

The new compact symmetric design has a working distance of ~ 20 mm at both sides and 60° angular aperture. Hence, with optimal optical design for ruby fluorescence image collection setup with a similar small focal length objective at both sides, one may get high-resolution fluorescence images at both sides of the SSDAC, providing more accurate estimates of displacement fields in the sample under complex load-shear pathways.

V. CONCLUSIONS

With symmetric angular opening and short working distance at both sides, the newly designed compact SSDAC facilities implement the recently developed methodologies for more accurate quantitative studies of plastic strain-induced phase transitions. The oblique angle XRD, possible with the new design, provides more accurate estimates of stress states under HPT. In addition, quantitative texture estimates are also more accurate with larger convergence of pole figures by collecting XRD data at different ω angles. With shorter and symmetric working distance, the SSDAC can be used for spatially resolved Raman mapping and displacement field measurements at both sides, providing more insight into the processes happening under high-pressure torsion. The compact size of SSDAC is easy to carry and use at laboratory-based and synchrotron experimental facilities. Although the newly designed SSDAC has several advantages over other existing designs of SDAC, there is always scope of future improvements. One of the limitation of the present design is limited lateral opening, which does not allow radial diffraction measurements perpendicular to load axis. Although the DAC is not meant for such measurements, incorporation of larger lateral opening in the future design will be an added advantage. Larger lateral opening in future designs will also be useful for more advanced novel techniques, such as 3DXRD and diffraction contrast tomography (DCT), providing more detailed *in situ* information about internal structure, strain heterogeneities,

and grain mapping in polycrystalline samples during shear at high pressures.

ACKNOWLEDGMENTS

We acknowledge the institutional support for this development work. We thank Mr. M. M. Tandel, Dr. Velaga Srihari, Dr. K. Phaneendra, Dr. M. Modak, and Dr. Abhilash Dwivedi for user support at the ECXRD beamline (BL-11), Indus-2. We also thank Mr. A. K. Poswal for his valuable suggestions and for critically reviewing the design of the cell. The author, K. K. Pandey thanks Professor Valery I. Levitas, ISU, USA for introducing him to the research field of plastic strain-induced phase transitions during his post-doctoral tenure at ISU, USA.

AUTHOR DECLARATIONS

Conflict of Interest

The authors have no conflicts to disclose.

Author Contributions

K. K. Pandey: Conceptualization (equal); Data curation (equal); Formal analysis (equal); Investigation (equal); Methodology (equal); Validation (equal); Writing – original draft (equal); Writing – review & editing (equal). **H. K. Poswal:** Conceptualization (equal); Data curation (equal); Formal analysis (equal); Investigation (equal); Methodology (equal); Validation (equal); Writing – original draft (equal); Writing – review & editing (equal).

DATA AVAILABILITY

The data presented in this manuscript are available from the corresponding author upon reasonable request.

REFERENCES

- ¹K. Edalati *et al.*, “Nanomaterials by severe plastic deformation: Review of historical developments and recent advances,” *Mater. Res. Lett.* **10**(4), 163–256 (2022).
- ²M. Durand-Charre, *La Microstructure des aciers et des fontes [Microstructure of Steels and Cast Irons]* (Gense et Interpretation Ed. SIRPE, Paris, 2003).

- ³J. Lapérouse, "Metallurgy: Early metallurgy in mesopotamia," in *Encyclopaedia of the History of Science, Technology, and Medicine in Nonwestern Cultures*, 2nd ed., edited by H. Selin (Springer-Verlag, Berlin, 2008), p. 1632.
- ⁴M. Durand-Charre, *Damascus Andpatter-Weldedsteels, Forging Blades Since the Iron Age* (LesUlis: EDP Sciences, 2014).
- ⁵R. Tewari, "The origins of iron working in India: New evidence from the central Ganga plain and the Eastern Vindhya," *Antiquity* **77**(297), 536–544 (2003).
- ⁶R. Z. Valiev, Y. Estrin, Z. Horita *et al.*, "Producing bulk ultrafine-grained materials by severe plastic deformation," *JOM* **58**, 33–39 (2006).
- ⁷V. M. Segal, "Review: Modes and processes of severe plastic deformation (SPD)," *Materials* **11**, 1175 (2018).
- ⁸P. W. Bridgman, "Effects of high shearing stress combined with high hydrostatic pressure," *Phys. Rev.* **48**, 825–847 (1935).
- ⁹P. W. Bridgman, *Studies in Large Plastic Flow and Fracture* (McGraw-Hill, New York, NY, 1952).
- ¹⁰K. Edalati and Z. Horita, "A review on high-pressure torsion (HPT) from 1935 to 1988," *Mater. Sci. Eng. A* **652**, 325–352 (2016).
- ¹¹A. P. Zhilyaev and T. G. Langdon, "Using high-pressure torsion for metal processing: Fundamentals and applications," *Prog. Mater. Sci.* **53**, 893–979 (2008).
- ¹²K. Edalati, D. J. Lee, T. Nagaoka, M. Arita, H. S. Kim, Z. Horita, and R. Pippin, "Real hydrostatic pressure in high-pressure torsion measured by bismuth phase transformations and FEM simulations," *Mater. Trans.* **57**(4), 533–538 (2016).
- ¹³C. E. Weir, E. R. Lippincott, A. Van Valkenburg, and E. N. Bunting, "Infrared studies in the 1- to 15-micron region to 30,000 atmospheres," *J. Res. Nat. Bur. Stand. Sect. A* **63**, 55–62 (1959).
- ¹⁴V. V. Aksenenkov, V. D. Blank, Y. S. Konyayev *et al.*, "Investigation of phase equilibria in a diamond chamber for shear at pressures up to 25.0 GPa," *Phys. Met. Metallogr.* **57**, 159–162 (1984).
- ¹⁵V. D. Blank, Y. S. Konyayev, A. I. Kuznetsov *et al.*, "Diamond chamber for examining the effects of shear deformation on the structure and properties of solids at pressures up to 43 GPa," *Instrum. Exp. Tech.* **27**, 1240–1242 (1984).
- ¹⁶V. I. Levitas, Y. Ma, J. Hashemi, M. Holtz, and N. Guven. Strain-induced disorder, phase transformations, and transformation-induced plasticity in hexagonal boron nitride under compression and shear in a rotational diamond anvil cell: In situ x-ray diffraction study and modeling. *J. Chem. Phys.* **125**, 044507 (2006).
- ¹⁷V. D. Blank, M. Y. Popov, and B. A. Kulnitskiy, "The effect of severe plastic deformations on phase transitions and structure of solids," *Mater. Trans.* **60**, 1500–1505 (2019).
- ¹⁸J. H. Chen, L. Li, D. Weidner, and M. Vaughan, "Deformation experiments using synchrotron X-rays: In situ stress and strain measurements at high pressure and temperature," *Phys. Earth Planet. Inter.* **143–144**, 347–356 (2004).
- ¹⁹N. V. Novikov, S. B. Polotnyak, L. K. Shvedov, and V. I. Levitas, "Regularities on phase transformations and plastic straining of materials in compression and shear on diamond anvils: Experiments and theory," *J. Superhard Mat.* **21**(3), 36–48 (1999).
- ²⁰Y. B. Wang, W. B. Durham, I. C. Getting, and D. J. Weidner, "The deformation-DIA: A new apparatus for high temperature triaxial deformation to pressures up to 15 GPa," *Rev. Sci. Instrum.* **74**, 3002–3011 (2003).
- ²¹S. A. Hunt, D. J. Weidner, R. J. McCormack, M. L. Whitaker, E. Bailey, L. Li, M. T. Vaughan, and D. P. Dobson, "Deformation T-Cup: A new multi-anvil apparatus for controlled strain-rate deformation experiments at pressures above 18 GPa," *Rev. Sci. Instrum.* **85**, 085103 (2014).
- ²²N. B. Novikov, L. K. Shvedov, Y. N. Krivosheya, and V. I. Levitas, "New automated shear cell with diamond anvils for in situ studies of materials using X-ray diffraction," *J. Superhard Mater.* **37**(1), 1–7 (2015).
- ²³R. Nomura, S. Azuma, K. Uesugi, Y. Nakashima, T. Irifune, T. Shinmei, S. Kakizawa, Y. Kojima, and H. Kadobayashi, "High-pressure rotational deformation apparatus to 135 GPa," *Rev. Sci. Instrum.* **88**, 044501 (2017).
- ²⁴Y. Ma, E. Selvi, V. I. Levitas, and J. Hashemi, "Effect of shear strain on the $\alpha - \epsilon$ phase transition of iron: A new approach in the rotational diamond anvil cell," *J. Phys.: Condens. Matter* **18**, S1075–S1082 (2006).
- ²⁵C. Ji, V. I. Levitas, H. Zhu, J. Chaudhuri, A. Marathe, and Y. Ma, "Shear-induced phase transition of nanocrystalline hexagonal boron nitride to wurtzitic structure at room temperature and lower pressure," *Proc. Natl. Acad. Sci. U. S. A.* **109**, 19108 (2012).
- ²⁶Y. Gao, Y. Ma, Q. An, V. Levitas, Y. Zhang, B. Feng, J. Chaudhuri, and W. A. Goddard, "Shear driven formation of nano-diamonds at sub-gigapascals and 300 K," *Carbon* **146**, 364–368 (2019).
- ²⁷Y. Nishihara, D. Tinker, T. Kawazoe, Y. Xu, Z. Jing, K. N. Matsukage, and S.-i. Karato, "Plastic deformation of wadsleyite and olivine at high-pressure and high-temperature using a rotational Drickamer apparatus (RDA)," *Phys. Earth Planet. Inter.* **170**, 156–169 (2008).
- ²⁸T. Kawazoe, T. Ohuchi, N. Nishiyama, Y. Nishihara, and T. Irifune, "Preliminary deformation experiment of ringwoodite at 20 GPa and 1700 K using a D-DIA apparatus," *J. Earth Sci.* **21**, 517–522 (2010).
- ²⁹L. Li, D. Weidner, P. Raterron, J. Chen, M. Vaughan, S. Mei, and B. Durham, "Deformation of olivine at mantle pressure using the D-DIA," *Eur. J. Mineral.* **18**, 7–19 (2006).
- ³⁰W. B. Durham, S. Mei, D. L. Kohlstedt, L. Wang, and N. A. Dixon, "New measurements of activation volume in olivine under anhydrous conditions," *Phys. Earth Planet. Inter.* **172**, 67–73 (2009).
- ³¹H. K. Mao, B. Chen, J. Chen, K. Li, J.-F. Lin, W. Yang, and H. Zheng, "Recent advances in high-pressure science and technology," *Matter Radiat. Extremes* **1**, 59 (2016).
- ³²K. Edalati, I. Taniguchi, R. Floriano, and A. D. Luchessi, "Glycine amino acid transformation under impacts by small solar system bodies, simulated via high-pressure torsion method," *Sci. Rep.* **12**, 5677 (2022).
- ³³V. I. Levitas, "Continuum mechanical fundamentals of mechanochemistry," *High Pressure Surface Science and Engineering* (Institute of Physics, Bristol, 2004), Vol. 159–292.
- ³⁴V. I. Levitas, "High-pressure mechanochemistry: Conceptual multiscale theory and interpretation of experiments," *Phys. Rev. B* **70**(18), 184118 (2004).
- ³⁵V. I. Levitas, "Phase transformations, fracture, and other structural changes in inelastic materials," *Int. J. Plast.* **140**, 102914 (2021).
- ³⁶V. I. Levitas, "Recent in situ experimental and theoretical advances in severe plastic deformations, strain-induced phase transformations, and microstructure evolution under high pressure," *Mater. Trans.* **64**(8), 1866–1878 (2023).
- ³⁷F. Lin, V. I. Levitas, K. K. Pandey, S. Yesudhas, and C. Park, "In-situ study of rules of nanostructure evolution, severe plastic deformations, and friction under high pressure," *Mater. Res. Lett.* **11**(9), 757–763 (2023).
- ³⁸V. I. Levitas, "High-pressure phase transformations under severe plastic deformation by torsion in rotational anvils," *Mater. Trans.* **60**(7), 1294–1301 (2019).
- ³⁹K. K. Pandey and V. I. Levitas, "In situ quantitative study of plastic strain-induced phase transformations under high pressure: Example for ultra-pure Zr," *Acta Mater.* **196**, 338–346 (2020).
- ⁴⁰G. L. Kinsland and W. A. Bassett, "Modification of the diamond cell for measuring strain and the strength of materials at pressures up to 300 kilobar," *Rev. Sci. Instrum.* **47**, 130–133 (1976).
- ⁴¹R. J. Hemley, H. K. Mao, G. Shen, J. Badro, P. Gillet, M. Hanfland, and D. Häusermann, *Science* **276**, 1242–1245 (1997).
- ⁴²A. K. Singh, H. K. Mao, J. Shu, and R. J. Hemley, *Phys. Rev. Lett.* **80**, 2157–2160 (1998).
- ⁴³V. I. Levitas, A. Dhar, and K. K. Pandey, "Tensorial stress-plastic strain fields in $\alpha - \omega$ Zr mixture, transformation kinetics, and friction in diamond-anvil cell," *Nat. Commun.* **14**, 5955 (2023).
- ⁴⁴See <http://merkel.texture.rocks/RDX/index.php?n=Maud.DataCoverageInAxialDiffractionExperiments>
- ⁴⁵R. Boehler and K. De Hantsetters, "New anvil designs in diamond-cells," *High Pressure Res.* **24**(3), 391–396 (2004).
- ⁴⁶H. K. Mao, J. Xu, and P. M. Bell, "Calibration of the ruby pressure gauge to 800 kbar under quasi-hydrostatic conditions," *J. Geophys. Res.* **91**, 4673, <https://doi.org/10.1029/jb091ib05p04673> (1986).
- ⁴⁷Y. Akahama and H. Kawamura, "Pressure calibration of diamond anvil Raman gauge to 310 GPa," *J. Appl. Phys.* **100**, 043516 (2006).
- ⁴⁸K. K. Pandey and V. I. Levitas, "Displacement field measurements in traditional and rotational diamond anvil cells," *J. Appl. Phys.* **129**, 115901 (2021).
- ⁴⁹H. M. Rietveld, "A profile refinement method for nuclear and magnetic structures," *J. Appl. Cryst.* **2**, 65–71 (1969).

⁵⁰M/s. Somdev Instruments Pvt. Ltd., Jaipur (India), Email: somdevinstruments@gmail.com.

⁵¹K. K. Pandey, H. K. Poswal, A. K. Mishra *et al.*, “Energy-dispersive X-ray diffraction beamline at Indus-2 synchrotron source,” *Pramana* **80**, 607–619 (2013).

⁵²L. Lutterotti Maud, “A Rietveld analysis program designed for the internet and experiment integration,” *Acta Cryst. Sect. A* **56**, s54 (2000).

⁵³V. I. Levitas, M. Kamrani, and B. Feng, “Tensorial stress–strain fields and large elastoplasticity as well as friction in diamond anvil cell up to 400 GPa,” *NPJ Comput. Mater.* **5**, 94 (2019).